Arabian Journal of Chemistry (2021) **14**, 102924

King Saud University

Arabian Journal of Chemistry

www.ksu.edu.sa
www.sciencedirect.com

ORIGINAL ARTICLE

Development of porous, antibacterial and biocompatible GO/n-HAp/bacterial cellulose/ β-glucan biocomposite scaffold for bone tissue engineering

Muhammad Umar Aslam Khan [a,b,c,*], Sajjad Haider [d], Adnan Haider [e,*], Saiful Izwan Abd Razak [b,f], Mohammed Rafiq Abdul Kadir [b], Saqlain A Shah [g], Aneela Javed [h], Imran Shakir [i], Ateyah A. Al-Zahrani [d]

[a] *Department of Polymer Engineering and Technology, University of the Punjab, Lahore 54590, Pakistan*
[b] *School of Biomedical Engineering and Health Sciences, Faculty of Engineering, Universiti Teknologi Malaysia, 81300 Skudai, Johor, Malaysia*
[c] *School of Biomedical Engineering, Med-X Research Institute, Shanghai Jiao Tong University (SJTU), 1954 Huashan Road, Shanghai 200030, China*
[d] *Department of Chemical Engineering, College of Engineering, King Saud University, P.O BOX 800, Riyadh 11421, Saudi Arabia*
[e] *Department of Biological Sciences, National University of Medical Sciences, Rawalpindi, Punjab, Pakistan*
[f] *Centre for Advanced Composite Materials, Universiti Teknologi Malaysia, 81300 Skudai, Johor, Malaysia*
[g] *Nanotechnology Lab, Department of Physics, Forman Christian College (University) Lahore, Pakistan*
[h] *Department of Healthcare Biotechnology, Atta ur Rahman School of Applied Biosciences, National University of Sciences and Technology, Islamabad Pakistan*
[i] *Sustainable Energy Technologies Center, College of Engineering, King Saud University, P.O.BOX, 800, Riyadh 11421, Saudi Arabia*

Received 25 August 2020; accepted 29 November 2020
Available online 9 December 2020

KEYWORDS

Biocompatible;
Bacterial cellulose;
β-Glucan nanocomposite;
Tissue engineering

Abstract Due to their potential renewable materials-based tissue engineering scaffolds has gained more attention. Therefore, researchers are looking for new materials to be used as a scaffold. In this study, we have focused on the development of a nanocomposite scaffold for bone tissue engineering (using bacterial cellulose (BC) and β-glucan (β-G)) *via* free radical polymerization and freeze-drying technique. Hydroxyapatite nanoparticles (n-HAp) and graphene oxide (GO) were added as

* Corresponding authors at: Department of Polymer Engineering and Technology, University of the Punjab, Lahore 54590, Pakistan (M.khan) and Department of Biological Sciences, National University of Medical Sciences, Rawalpindi, Punjab, Pakistan (A. Haider)
E-mail addresses: umar007khan@gmail.com (M. Umar Aslam Khan), adnan_phd@outlook.com (A. Haider).
Peer review under responsibility of King Saud University.

Production and hosting by Elsevier

https://doi.org/10.1016/j.arabjc.2020.102924

reinforcement materials. The structural changes, surface morphology, porosity, and mechanical properties were investigated through spectroscopic and analytical techniques like Fourier transformation infrared (FT-IR), scanning electron microscope (SEM), Brunauer–Emmett-Teller (BET), and universal testing machine Instron. The scaffolds showed remarkable stability, aqueous degradation, spongy morphology, porosity, and mechanical properties. Antibacterial activities were performed against gram -ive and gram + ive bacterial strains. The BgC-1.4 scaffold was found more antibacterial compared to BgC-1.3, BgC-1.2, and BgC-1.1. The cell culture and cytotoxicity were evaluated using the *MC3T3*-E1 cell line. More cell growth was observed onto BgC-1.4 due to its uniform interrelated pores distribution, surface roughness, better mechanical properties, considerable biochemical affinity towards cell adhesion, proliferation, and biocompatibility. These nanocomposite scaffolds can be potential biomaterials for fractured bones in orthopedic tissue engineering.

1. Introduction

Bone is a highly porous vibrant tissue that is known for its possible skeleton property to protect the body's soft tissues and organs. It serves as a mineral supplying and blood production reservoir (Khan et al., 2020a,b,c; Soundarya et al., 2018). Bone damage is very common these days due to accidents, trauma, and diseases. Osteomyelitis is a common bone microbial disease that is triggered *via* bacterial or fungal infiltration. Staphylococcus aureus is the most popular microbe that leads to infection during surgery or implantation like hip replacement or repair of bone fracture (General & Welfare, 2013; Thévenin-Lemoine et al., 2016; Wiggli et al., 2017). Osteomyelitis also affects children's long bones such as arms or legs, although it usually occurs in adults on the neck, spine, and feet. Bone infection, if not handled carefully, can grow over a long period and may permanently damage the bone (Masters et al., 2019; Skrabl-Baumgartner et al., 2019). Biomedical procedures that are essential during trauma and fracture can't cure these deficiencies immediately. Bone tissue engineering is an innovative approach for the repair and treatment of damaged bone tissue (Hu et al., 2019). Porous scaffolds are three-dimensional potential biomaterials with high water-holding capacity, similarity to the extracellular matrix (ECM), and mechanism of cell adhesion and proliferation to compensate for bone defects. However, until care about Osteomyelitis type infections is not considered such approaches will not be successful. Therefore, the development of appropriate material and methodology for the fabrication of porous, biodegradable, biocompatible, and antibacterial scaffold is essential not only for bone regeneration to mimic the instinctive structures of bone tissue but also to tackle the pathogen infections that occur during the biomedical procedure for the bone-implant (Fang et al., 2019; Khan et al.; Saravanan et al., 2017; Shah et al., 2016). Numerous materials and methods were adopted to fabricate the scaffold synthesis for bone tissue engineering by employing polymers (both natural and synthetic) and ceramics (hydroxyapatite, bioglasses, silica, and titian, etc.). The selection of materials is a crucial step because the features of any material can decide the overall properties of the scaffold. In recent decades, biopolymers have gained considerable attention in tissue engineering due to their biodegradation, non-toxicity, and inherent antibacterial and biocompatible activities (Aslam et al., 2020; Khan et al., 2020a,b,c). β-G is an ideal biodegradable biopolymer for cell attachment substrates, cell growth, and the preservation of the distinct phenotype. β-G is a naturally occurring biodegradable biopolymer. It has several pharmaceuticals, medicinal, and anti-bacterial features that could lead to its ultimate applications in tissue engineering.Though β-G uses in pharmaceutical materials as wound healing and drug delivery carriers to support biological activities have been reported in the literature but not much has been done on its application in tissue engineering (Khan et al., 2020a). BC, a biopolymer, is another very effective polymer produced from certain Gram - ive bacteria. Its chemical formulation is identical to plant cellulose, however, both have slightly different properties in terms of water holding capacity and mechanical strength (Ullah et al., 2016). BC has a nanofibrous microstructure having smaller fiber diameters, higher mechanical strength, cross-linking rate, water holding capacity, crystallinity, and moldability (Yamanaka et al., 1989). Various studies have confirmed the biocompatibility of BC and its composite materials. BC can't be biodegraded naturally by human enzymes, however, its biodegradation can be regulated by cellulases incorporation. These characteristics make BC a better choice in tissue engineering scaffolding (Torgbo & Sukyai, 2018). HAp is a well-known ceramic brittle material, known as bone cement, resembles natural bone components, and exhibits excellent biocompatibility (Askari et al., 2020). The properties of a scaffold such as porosity, pore size, water holding capacity, mechanical strength, and biodegradation can be controlled through polymeric/HAp ratios and synthesis methods. Graphene-based materials have been recognized due to their abundance and economical synthesis from graphite. It has many potential applications in electricity, electronics, molecular sensing, catalysis, and has recently been recognized in biomedical engineering such as nanomedicine, drug delivery, tissue engineering, and wound healing (Chung et al., 2013). Many different approaches have been used to fabricate porous biocompatible scaffolds from polymer and ceramic materials. For example, Maheshwari et al. synthesized PVA/HAp/PCL composite scaffolds and investigated their physicochemical and biological activity for potential application in bone regeneration. The developed scaffolds were found to be biocompatible showing good osteoblast (MG-63) cell line adhesion and proliferation. Furthermore, the MG-63 cells retained their morphology in the cultural media. (Maheshwari et al.,

2014). Sancilio et al. developed alginate/HAp nanocomposite scaffolds for bone tissue engineering. They observed that the scaffolds were biocompatible, and non-cytotoxic (Sancilio et al., 2018). Unnithan et al. reported osteogenic GO/hyaluronic acid/chitosan composite biomaterial for bone tissue engineering. During the in-vitro studies on this material, they found that the material showed a positive impact on biomineralization, and excellent biocompatibility to encourage osteogenesis (Unnithan et al., 2017). These studies, however, did not concentrate much on the antibacterial aspect of the scaffold. However, most natural polymer based scaffolds have low tensile strength and readily degrades in moist environment. To aovid degradation, these are gerenally crosslinked with crosslinkers, which are very toxic. Recently new approach was studied, where nautral biopolymers were grafting through free racial polymerization of arylicacid (AAc, a realtively non-toxic) to produce composite hydrogel with better mechanical properties (Khan et al., 2020a,b,c).

In this study, we have fabricated novel porous, antibacterial, biocompatible scaffolds having good mechanical strength for bone tissue engineering. The free-radical polymerization technique was used to graft *β*-G, and BC by decorating n-HAp and GO into the polymers network. The freeze-drying technique (at −40 °C) was used to fabricate porous scaffolds for hard tissue regeneration (Scheme 1). To the best of our knowledge, this formulation is never reported before.

2. Materials and methods

2.1. Chemicals and reagents

The barley flour (mesh size 20 mm) was bought from DSP Gokyo Food and Chemical Co. Ltd., Osaka Japan. Bacterial cellulose, acrylic acid (AAc), *N'*, N-methylene-bis-acrylamide (*N'*, N-MBA), n-HAp powder (< 100 nm particle size), graphene oxide (GO), phosphate buffer saline solution (PBS), and hydrochloric acid were obtained from Sigma-Aldrich, Selangor, Malaysia. All chemicals were of analytical grade and used without any purification.

2.2. Extraction and purification of β-glucan from barley floor

The extraction and purification of β-G ((1,3;1,4)-β-glucans) were conducted by a well-reported method with a slight modification (Wood et al., 1989). The fine barley flour (100 g) was dispersed into 500 mL deionized water. The pH of the slurry was adjusted at 10 using Na_2CO_3 (20%, v/w). The suspension was strongly stirred for 30 min at 45 °C. Then, the suspension was centrifuged at 18000 × g for 20 min at 4 °C and pH 4.5 to separate the precipitated protein. The separated protein was discarded and absolute ethanol was added into the suspension with equal quantity at slow stirring to get precipitated β-G. The suspension was centrifuged at 4000 × g for 15 min to recover precipitate and allowed at 4 °C overnight. It was then freeze-dried to get a fine powder of β-G. The powder was packed into an airtight glass jar for further usage.

2.3. Synthesis of the nanocomposite materials

The nanocomposites were synthesized by free radical polymerization as reported by Khan et al (Khan et al., 2020a,b,c). Briefly, 1 g of β-G and 1 g of BC with different amounts of GO (0.1, 0.2, 0.3 & 0.4 g) were dispersed into deionized water. Then, the solution was transferred to a two-neck round bottom flask under continuous heating for 2 min at 65 °C under the nitrogen atmosphere. After 30 min, 0.50 mL of AAc as a

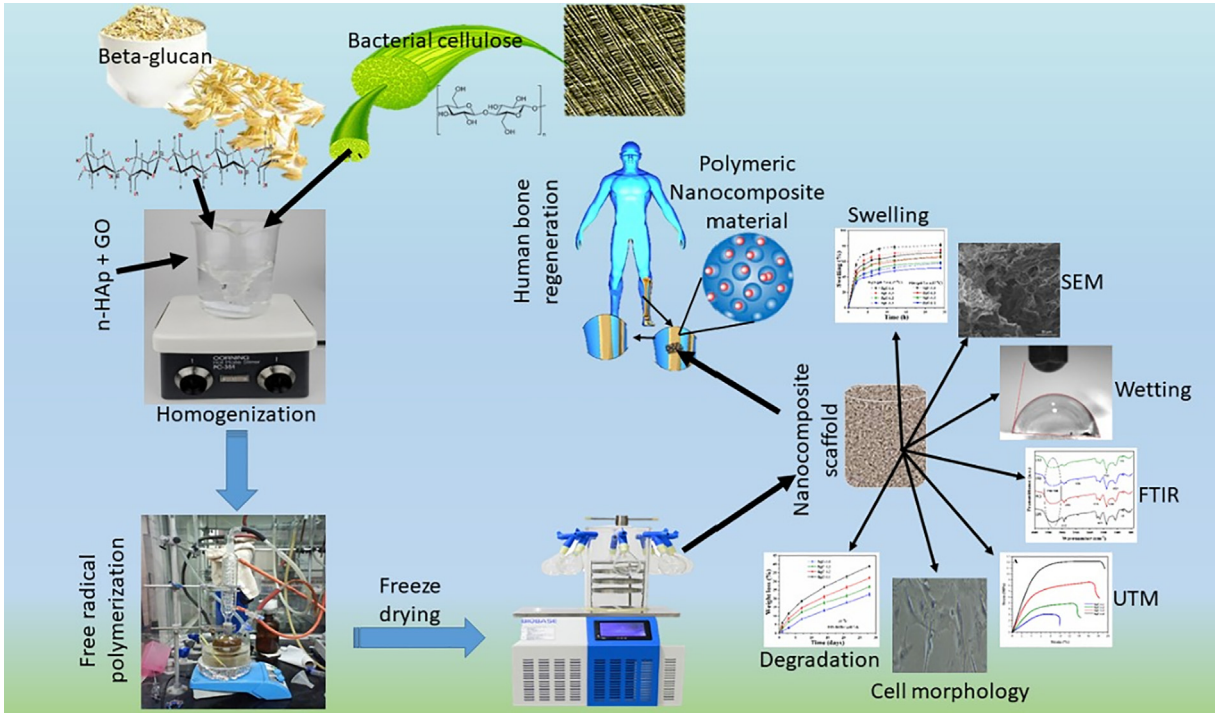

Scheme 1 Stepwise synthesis of the polymeric composite scaffolds for bone tissue engineering, from polymeric materials, GO, and HAp nanomaterials *via* free-radical polymerization and freeze-drying.

monomer and *N*, N-MBA as a crosslinker (0.05% of AAc) was added to the reaction media. After 45 min, 2.5 g of n-HAp powder was gradually added to the mixture with continuous stirring to obtain a homogenized mixture solution. Finally, 0.05 g of potassium persulfate was added to the mixture solution as an initiator. The mixture solution was heated at 65 °C for 3 h with continuous stirring. Hence, the grafting of AAc into β-B/BC was done by a free-radical polymerization reaction. The nanoparticles were engulfed by the polymeric network of grafted βG/BC at the end of reaction. Nitrogen gas was removed from the reaction media. The reaction media was allowed to cool untill room temperature. The reaction media was vacuum filtered and washed with excessive deionized water to eliminate unreacted chemicals and dried overnight at 55 °C in the oven. Then, 5 g of nanocomposite powder was dispersed into 10 mL of deionized water and filled into cylindrical molds (2 cm × 6 cm) to create a homogenized slurry. These molds were frozen at − 40 °C for 24 h and freeze-dried to obtain porous scaffolds. The details of chemicals have been described in Table 1 and the proposed structural chemistry is shown in Scheme 2. The scaffolds were coded as BgC-1.1, BgC-1.2, BgC-1.3, and BgC-1.4 due to the variable amounts of GO. The pore size and porosity of the scaffolds was analyzed using Brunauer–Emmett–Teller (Gemini II 2370 micromeritics) and image J software (Table 1).

2.4. Characterizations

FT-IR analysis for the determination of various functional groups was carried out by using Perkin-Elmer Diamond 1000 FT-IR spectrophotometer. The frequency range was 4000 to 400 cm^{-1} with 64 scans and 4.0 cm^{-1} resolution. The amorphous and crystalline behavior of scaffold samples was determined by the X-ray diffractometer (Bruker AXS D8 Advance XRD). The XRD data were obtained at a 40 kV and a 30 mA using Cu Kα radiation (1.540 Å). 2θ° was selected in the range of 20° to 80°. The fracture surface morphologies of the composite scaffolds, cell adhesion, and proliferation of cells onto the composite scaffold were investigated by scanning electron microscope ((SEM) (JEOL-JSM-6480) coupled with Energy dispersive spectroscopy (EDS) to determine the elemental analysis of the scaffold samples. The scaffolds were well dried and gold-sputtered before analysis. Brunauer–Emmett-Teller ((BET) Micromeritics Gemini II 2370) was used to determine the pore size and porosity of the scaffolds. Wetting properties of the scaffolds were measured using an XCA-50 contact-angle meter. The wetting analysis was performed by releasing water droplets (4 μL) over the scaffold surface. The surface was photographed at different time intervals. The analysis was carried out in triplicate. The mechanical properties of the scaffolds were analyzed by a universal mechanical testing machine ((UTM (Testometrics, United Kingdom)) with a loading rate of 10 mm/min. The obtained load–displacement data from the compressive stress–strain curve was used to calculate Young's modulus and other mechanical properties. The mechanical testing was carried out in triplicate.

2.5. Swelling and water uptake

The swelling of the dried scaffolds was recorded by immersing the scaffolds separately into the PBS buffer solution and deionized water (pH 7.4) at 37°C. The scaffolds were taken out from both media at regular intervals. The experiment was carried out untill 24 h. The excess BPS and water were removed carefully from the scaffold by tissue paper. The swelled scaffolds were weighed and the percentage swelling of the scaffolds was calculated by the following equation (1). Each data was recorded in triplicate.

$$\textbf{\textit{Swelling}}(\%) = \frac{W_f - W_0}{W_0} \times 100 \quad (1)$$

Whereas: W_f = final weight and W_0 = Initial weight

To measure the water retention of the scaffolds, the dried scaffolds were separately immersed in deionized water at various temperatures (35, 37, 39 ℃) The scaffolds were removed from the water at a predetermined time. The excess water was removed carefully from the scaffold by tissue paper. These scaffolds were then weighed. The water retention was obtained by Equation (2). Each data was recorded in triplicate.

$$\textbf{\textit{WaterUptake}}(\%) = \frac{W_w - W_d}{W_w} \times 100 \quad (2)$$

Whereas: W_w = wet scaffold and W_d = dry scaffold

2.6. Degradation

In-vitro degradation (in terms of weight loss) of the scaffolds was conducted in PBS solution (7.4 pH) at 37 °C. Dried scaffolds were separately weighed and immersed in PBS. After a predetermined time, the scaffolds were gently taken out of the PBS solution, placed into an oven at 55 °C for 1 h, and weighed. The percentage of the degradation was determined for 30 days. The PBS solution was replaced with fresh PBS solution after every two days. The weight loss of the scaffolds was determined by Eq. (2). Each data was recorded in triplicate.

$$\textbf{\textit{Degradation}}(\%) = \frac{W_o - W_t}{W_o} \times 100 \quad (3)$$

Where: W_t = weight after incubation at a time "t" and Wo = weight at "0".

Table 1 Composition, pore size, and porosity of the nanocomposite scaffolds.

Scaffold Sample	β-G (g)	BC (g)	n-HAp (g)	GO (mg)	Pore size (μm)	Porosity (%)
BgC-1.1	1	1	2.5	0.1	357 ± 6.34	73 ± 2.23
BgC-1.2	1	1	2.5	0.2	293 ± 2.92	61 ± 5.67
BgC-1.3	1	1	2.5	0.3	185 ± 2.81	53 ± 2.91
BgC-1.4	1	1	2.5	0.4	127 ± 3.42	47 ± 1.26

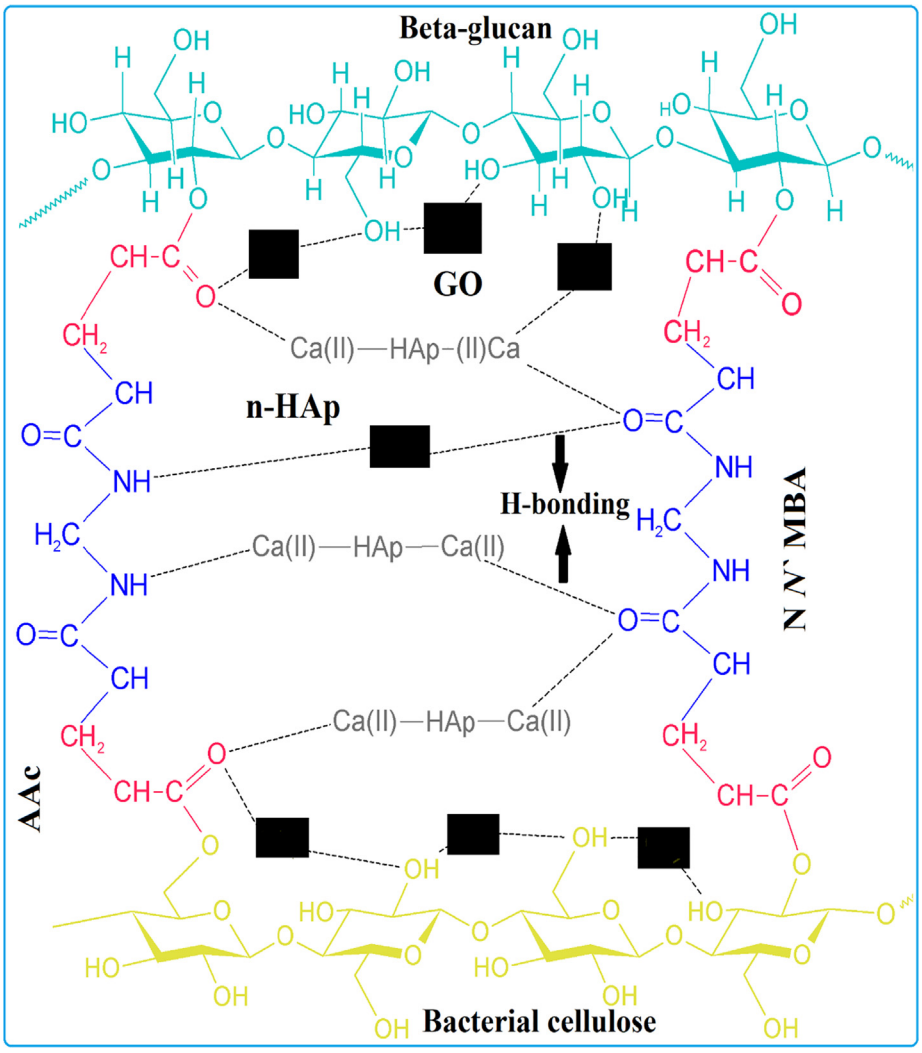

Scheme 2 The proposed interactive chemistry of the components (β-G, BC, n-HAp, GO, acrylic acid, and *N'*, N-methylene-bis-acrylamide) of the nanocomposite scaffolds.

2.7. Anti-microbial activities

Antibacterial activity of the scaffolds against Gram + ive *Staphylococcus aureus* (ATCC-29213), and Gram-ive *P. aeruginosa* (ATCC-27853) and *Escherichia coli* (ATCC-15224) was investigated by a well-reported disc diffusion method (Khan et al., 2020a). An equal amount (20 mL) of hot agar was poured into Petri dishes and let it solidified. Then, bacterial culture was spread uniformly over the solidified agar by a sterile cotton swab. After this, 85 µL of the pure slurry of scaffolds was separately dropped over each Petri dish and incubated for 24 h at 37 °C. The zones of inhibition were measured in millimeters (mm) using a meter ruler. Each data was recorded in triplicate (Bauer, 1966).

2.8. In vitro studies

2.8.1. Cell culture and morphological analyses

Mouse pre-osteoblast (*MC3T3-E1*) cell-line was purchased from ATCC (Manassa, VA, USA) and preserved according to ATCC recommendations. Cell culture and cell morphology assays were conducted against scaffolds and well plates coated with 0.1% gelatin solution. The well plate coated with 0.1% gelatin was considered as a positive control. These plates were incubated under standard *in-vitro* conditions (at 37 °C, 5% CO_2) and recommended medium formulation of alpha modified MEM medium (with ribonucleosides and 2 mM L-glutamine(Cat# A1049001 Gibco™)). The complete medium was prepared by adding 10% fetal bovine serum (FBS # 10270106, Gibco™) and 1:100 volumes of 100 Pen/Strep solutions (Cat# 15140122, Gibco™). The density of *MC3T3-E1* cell lines was considered to be 5000 cells per cm^2 in a 100 mm culture plate. The pre-osteoblast cells were cultured over the composite bioactive scaffolds (2 mg/mL) for 24, 48, and 72 h. After the stipulated period, the cell lines were washed with PBS to remove unattached cells and particles. Absolute ethanol was used to fix the cultured cells (5 min at room temperature). These fixed scaffolds were dried well and gold-sputtered before analysis. The SEM micrographs of the cell culture were taken using an accelerating voltage of 5 kV with an operating pressure of 7×10^{-2} bar. The deposition current was 20 mA for

2.0 min. Cell morphologies were investigated under the Nikon ECLIPS TS100 fluorescence microscope using a 488 nm excitation filter. Vital dye like Fluorescein diacetate (FDA) was used to avoid the background interference in microscopy created by scaffold coating. FDA is a vital dye that allow only living cells and not the coating material to give green fluorescence under the fluorescence microscope's 488 nm excitation filter. Before, microscopic analysis, FDA stock solution was prepared according to manufacturer's instructions. 1.0 mL of Dimethyl sulfoxide (DMSO) was mixed with 0.5 mg of FDA (Sigma Aldrich, Taufkirchen, Germany). The working solution was prepared in the serum-free medium using FDA stock. The working medium was loaded on cells and allowed to absorb the dye at room temperature for 2 min. The excess FDA solution was removed from the cells by briefly rinsing the cells with 1X PBS (Phosphate Buffer Saline: 137 mM NaCl, 2.7 mM KCl, 4.3 mM Na_2HPO_4, 1.47 mM KH_2PO_4). Finally, the cell morphologies were imaged under the microscope.

2.8.1.1. Cell viability and cytotoxicity using neutral red (NR) assay. Neutral Red (NR) assay was used to measure cell viability and cytotoxicity. The mouse *MC3T3-E1* cell line was purchased from ATCC (Manassa, VA, USA). The NR assay was employed by seeding cells in 12 well plates. The density of *MC3T3-E1* cell lines was considered to be 5000 cells per cm^2 in a 100 mm culture of 24 well plates with different scaffolds concentrations (0.125–2.00 mg/mL). These were incubated under a humid atmosphere (95% humidity), 5% CO_2 at 37 °C for 24 h (in triplicate)). The wells of each concentration were assayed with NR assay as described by Repetto *et al* (Repetto, Del Peso, & Zurita, 2008). Before assay, the medium was filtered with a 0.45 µm syringe filter to remove undissolved debris. The cells were de-stained in a de-staining solution (50% distilled water, 49% absolute ethanol, and 1% glacial acetic acid) for 10 min at 37 °C. The cells were then washed with 150 µL PBS (per well) by immersing the plate in PBS and removing the washing solution by gentle tapping. The optical density (OD) of the cells was measured with a microplate reader (Bio-Tek, ELx-800, USA) at a wavelength of 540 nm. The cell viability (%) was evaluated by Eq. (2).

$$\textbf{Cellviability}(\%) = \frac{\boldsymbol{OD_S}}{\mathbf{OD}_C} \times 100$$

2.8.1.2. Statistical analysis. The data were obtained in triplicate and presented as mean ± standard error (S.E.). Statistical data were analyzed *via* statistical software system (IBM, SPSS Statistics 21). Means and standard errors (mean ± S.E) were measured for each analysis and S.E values were presented as Y-error bars in the Figures. Error bars showed standard deviations ($p < 0.05$; size of sample $n = 3$). The T-test significances value calculated for cell viability was $p < 0.001$ and optical density was $p < 0.05$.

3. Results and discussion

3.1. FT-IR and XRD analysis

Fig. 1 shows the FTIR spectra of BC, *β*-G, GO,n-Hap (Fig. 1A), and composite scaffolds (Fig. 1B). The characteristic band positions BC, *β*-G, GO, and nHAp are shown in their spectra. Since these positions and their intensities might vary in the composite, hence these are discussed in detail for the composite. The broadband in the region of 3100–3500 cm^{-1} is attributed to the H-bonding stretching vibrations, which is the characteristic band of polysaccharides. Close observation of the band revealed that the intensity of the broadband increased with an increase in the amount of GO. This confirms the successful incorporation of GO into the polymeric network through H-bonding (Kamal et al., 2014; Modrogan et al., 2020). The bands at 1228 cm^{-1}, 1033 cm^{-1}, and 910 cm^{-1} are attributed to the C–O stretching of AAc and pyranose, O-H bending vibration of the pyranose, and pyranose rings, respectively. The appearance of these bands in the spectra of the nanocomposite scaffold confirms the grafting of β-G/BC through AAc (Srivastava & Kumar, 2013). The absorption bands at 2931 cm^{-1} and 2855 cm^{-1} are attributed to the stretching of $–CH_2$. The intensities of these bands increased from BgC-1.1 to BgC-1.4. This increase was attributed to the increased participation of $–CH_2$ groups in free radical polymerization (Liu et al., 2012; Muruganandi et al., 2018). The band at 1725 cm^{-1} is attributed to the C = O stretching vibration of the COOH group on GO. This is confirmed by the increase in the intensity of the band with an increase in the amount of GO into a nanocomposite scaffold. The absorption band at 1632 cm^{-1} was attributed to O-H vibrations of the water molecules (Muruganandi et al., 2018). The bands at 1026 cm^{-1}, 607, and 562 cm^{-1} represented the triply degenerated P-O stretching and O-P-O bending of HAp. The spectra also showed two characteristic bands in the regions of 540–610 cm^{-1} and 990–1110 cm^{-1} for Ca^+ and $PO_4^{\bar{3}}$ moieties of HAp (Khan et al., 2020a,b,c). Moreover, the appearance of HAp at 630 cm^{-1} presented –OH confirming HAp into a nanocomposite scaffold (Khan et al., 2020a; Khan et al., 2020b,c). Thus, it was concluded from the spectra that all the components interacted and bonded well with each other in the nanocomposite scaffold.

Fig. 1C illustrates the XRD diffraction scans of the composite scaffolds. The results indicated that crystalline HAp exists in the composite with phases as recorded in the ICDD database. The characteristic peaks of HAp were found at 2θ 30.1, 41.9, 44.6, 49.2, and 55.4 which are corresponding to the planes (002), (211), (130), (400), (213) and (004). The cell parameters of HAp calculated for the nanocomposite scaffold were a = b = 9.4000 and c = 6.9300 A^o and the average crystallite size was 23.29 nm. These values are in agreement with the standard data (PDF-4–932). The peak intensity of the HAp decreased due to the presence of polymeric components (amorphous phase BG, BC, AAc, and N'*N*-MBA) (Khan et al., 2020a,b,c). This could be attributed to the hiding effect of HAp by the polymer matrix. A broad peak observed at 2θ 21.6 to 24.5 is the characteristic peak of GO (Garg et al., 2017); (Long et al., 2019; Todica et al., 2014). It is also important to note that BC, *β*-G, and AAc all show their diffraction peaks of different intensity and broadness in this region. In the composite, these peak intensities varied only due to the increase in GO. However, the changes in the peak broadness are associated with the reduction in crystallinity due to the synthesis of BG-g-*β*-G polymeric composite through free radical polymerization. The above results indicated the presence of the GO and HAp in the polymeric network, and the

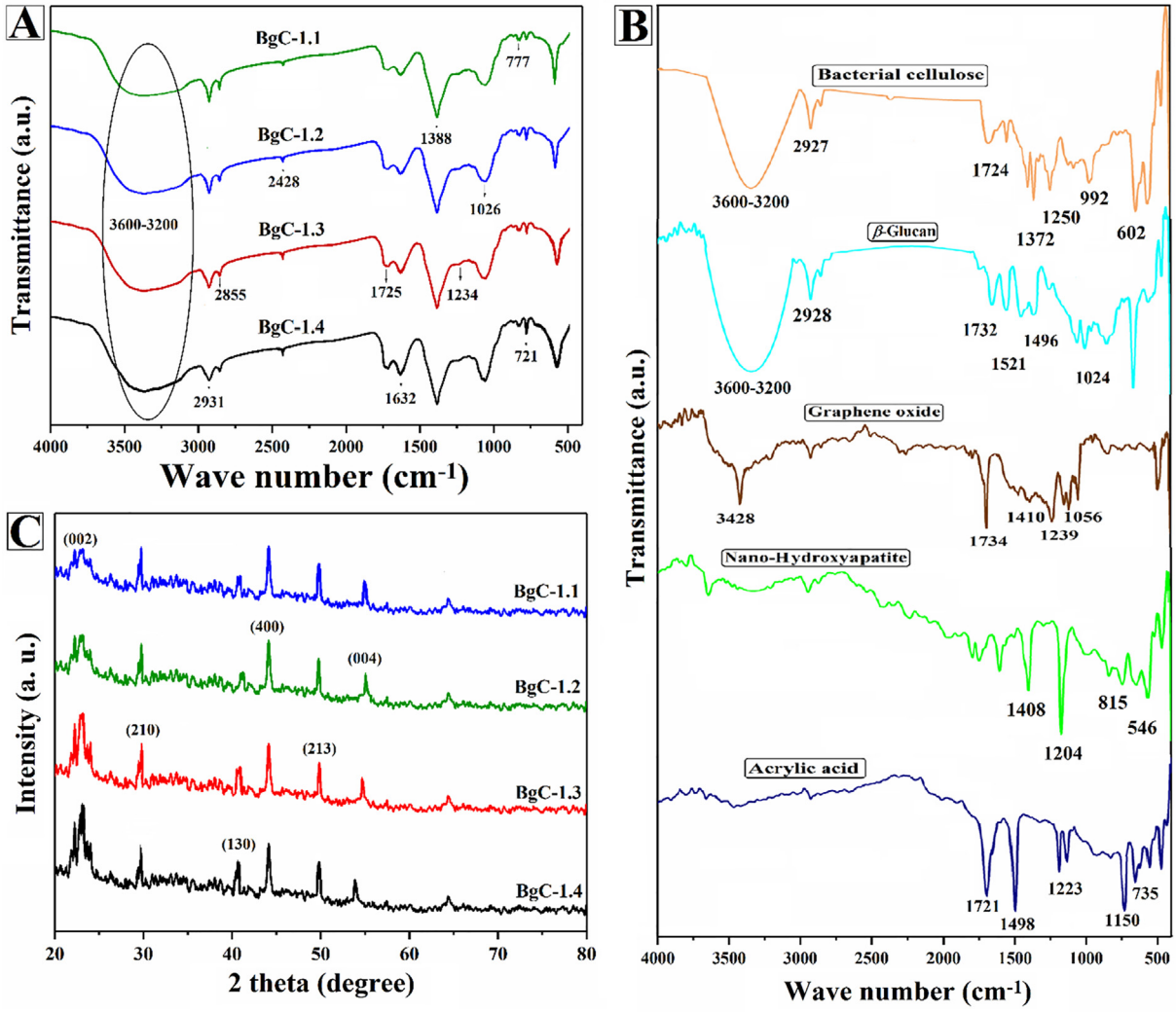

Fig. 1 FT-IR spectral profile of the different functional groups BC, β-G, GO, nHAp and nanocomposite scaffolds.

successful polymerization of βG, BC, AAc, and N'*N*-MBA (Schematic 2).

3.2. Morphological and energy dispersive X-Ray

The morphology of the scaffolds gives us significant information about the potential interaction of the cells with the scaffold. SEM morphological observations are therefore very important. Fig. 2 shows the SEM micrographs of the microstructural variations of the scaffolds. It is evident from the micrographs that all scaffolds possessed interconnected and homogeneous pore distribution. A highly interconnected porous structure of the scaffold is essential to retain tissue fluid and maintain high oxygen, nutrient, and waste permeability. Crosslinking and an increase in the amount of GO not only regularized porosity, pore size but also caused a decrease in porosity as well. The initial increased pore size and porosity of the nanocomposite scaffolds is attributed to the increased amount of retained water, which is presumably mostly non-bonded water (non-boned water is the water that freezes and creates pores). As the amount of the GO is increased; the free OH groups were occupied which led to the low hydrophilicity of the nanocomposite scaffolds, a low amount of non-bounded water, and hence decreased pore size. A critical porosity, pore size, and pore area result in a flexible scaffold with good cell adhesion, cell infiltration, proliferation, secretion of the extracellular matrix, and better *in vitro* degradation rate (Caló & Khutoryanskiy, 2015; Karahaliloglu et al., 2017), (Riahi et al., 2017). Porous ceramic implants that are fit for osteointegration have a pore size ranging from 100 to 350 μm. Since the pore size of the nanocomposite scaffolds is in the range of 127–357 μm (Table 1), which is in the range and/or greater than ceramics implants (100–350 μm), hence these are highly suitable for cell infiltration and cell adhesion. The chemical composition analysis of the composite scaffolds was conducted using X-ray differential spectroscopy (EDS) (Fig. 2 and Table 2). Carbon (C), oxygen (O), calcium (Ca), and phosphorus (P) elements were found in the composite scaffold (Table 2). The increasing spectral intensities of C and O were attributed to the increasing amount of GO. The peaks of Ca and P for HAp were also observed in the scan of the nanocomposite scaffolds (He, Liu, Yuan, & Lu, 2014; Yuan et al., 2013). The presence of these components indicates the incorporation of GO and HAp into the BG-g-β-G polymeric matrix.

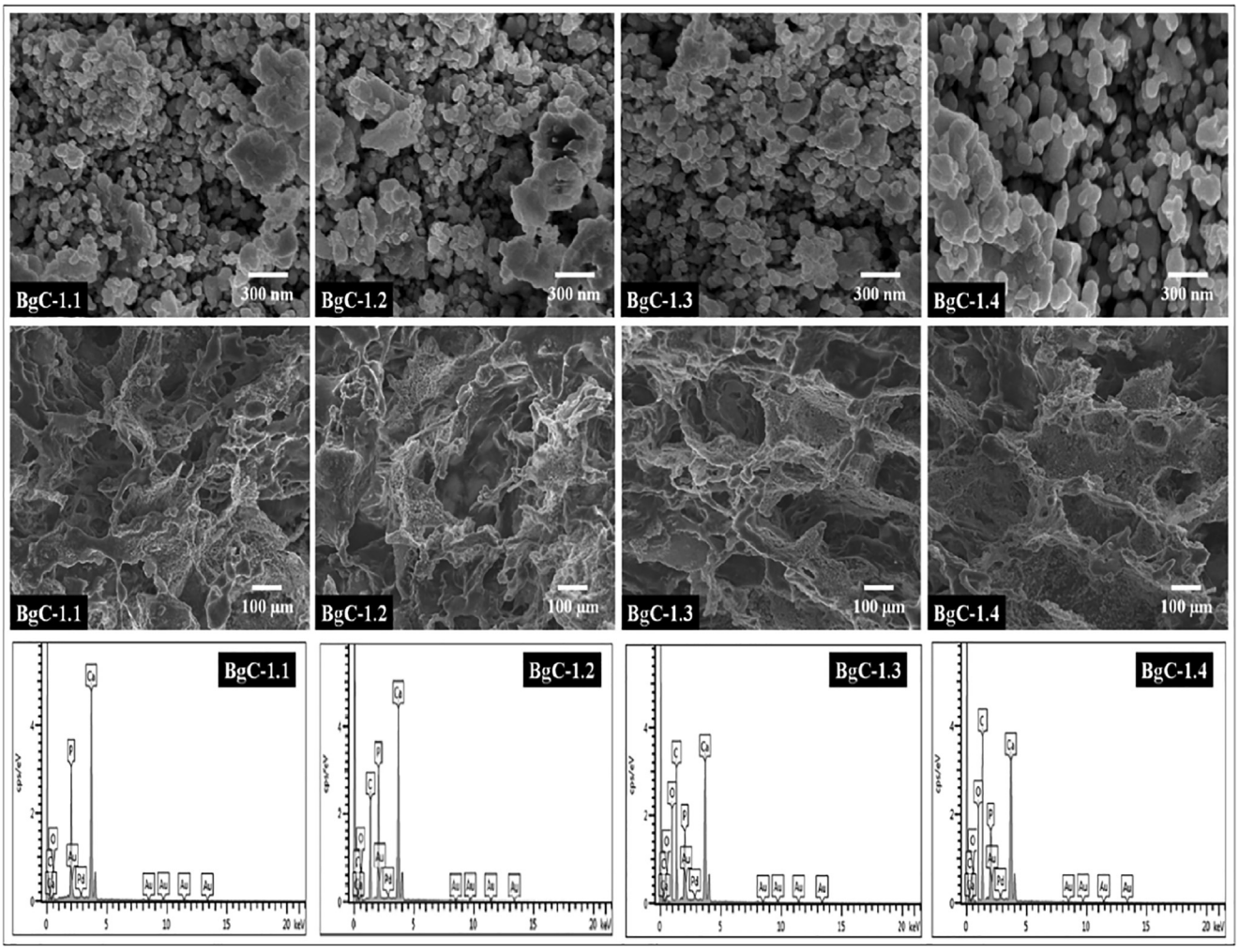

Fig. 2 SEM micrographs and EDS elemental analysis of the nanocomposite scaffolds.

3.3. Wetting

Wetting analysis is used to examine the hydrophilic or hydrophobic nature of the surface of a material. The lower the water content angle (WCA), the higher is the hydrophilicity and vice versa. The hydrophilic or hydrophobic character helps to understand surface response towards cellular behavior during biological activities. (Huang et al., 2016). Fig. 3 shows the wettability of the nanocomposite scaffolds as a function of the amount of GO. At 1 min, the WCA of the BgC-1.1, BgC-1.2, BgC-1.3 & BgC-1.4 scaffolds was 118.40°, 103.50°, 92.20°, and 79.70° and at 10 min was 95.60°, 82.00°, 77.20° & 64.10°, respectively. The increasing amount of GO shifted the surface hydrophilicity to hydrophobicity not only due to increased interactions of the oxygenated functionalities with polymer but also by regulating the porosity of the scaffolds (Wright et al., 2018), (Golafshan et al., 2018). However, at max. concentration of the GO; the surface of the scaffold was hydrophilic. The hydrophilic nature of the BgC-1.4 is attributed to the presence of the excessive unreactive GO in the scaffold. Many factors (stiffness, surface charge, surface chemistry, rough-

Table 2 Elemental analysis of the nanocomposite scaffolds.

Scaffold Sample	Elemental analysis (%)			
	Carbon (C)	Oxygen (O)	Calcium (Ca)	Phosphorus (P)
BgC-1.1	28.64	24.47	31.91	14.98
BgC-1.2	32.72	27.65	27.79	11.84
BgC-1.3	37.14	30.84	22.14	09.88
BgC-1.4	42.74	34.17	17.89	05.27

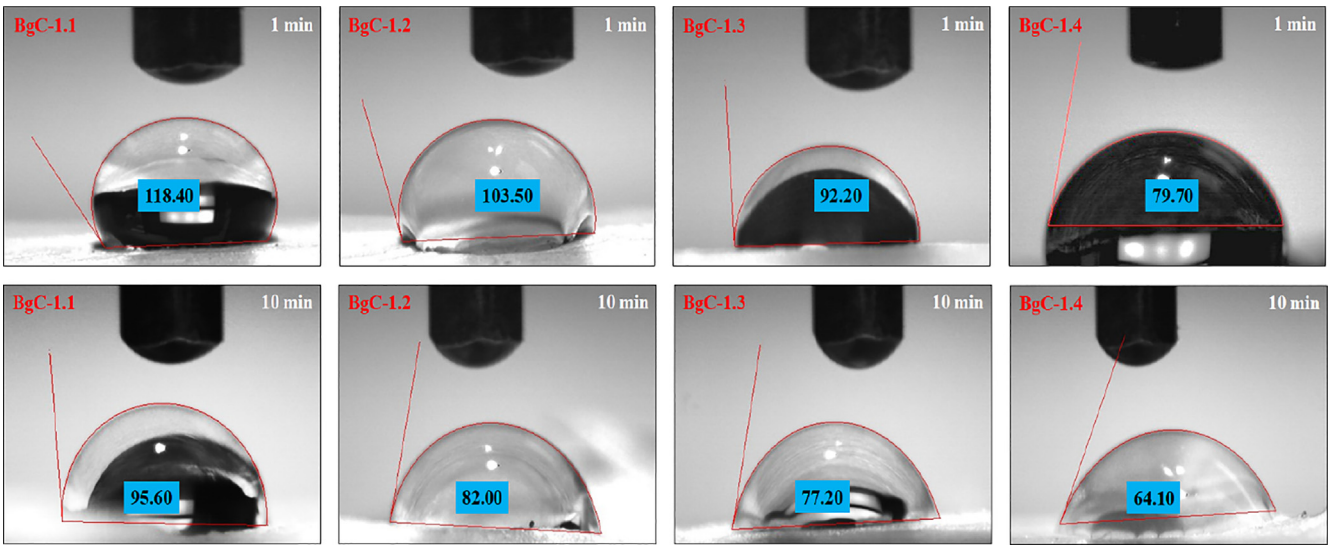

Fig. 3 Wetting analysis of the nanocomposite scaffold at 1 min and 10 min.

ness, or wettability) affect the interaction of the cells with the surface. More wettability some time negate adhesion of cell. However, an increased stiffness of the scaffold with a critical wettability may induce cell responses like adhesion and proliferation.

3.4. Porosity and pore area

Table. 1 shows the change in % porosity and pore size as a function of the amount of GO. The % porosity decreased as the amount of the GO was increased. The order of the decrease in % porosity was BgC-1.1 > BgC-1.2 > BgC-1.3 > BgC-1.4. Pore size also followed the same trend BgC-1.1 > BgC-1.2 > BgC-1.3 > BgC-1.4 (Table 1). Crosslinking and an increase in the amount of GO not only regularized pores and pore size but also caused a decrease in % porosity. The initially increased % porosity and pore size are attributed to the increased amount of retained water, which is presumably mostly non-bonded water (non-boned water is the water that freezes and creates pores). This non bonded water during freeze-drying evaporated, which led to an increase in the % porosity of the nanocomposite scaffold. As the amount of the GO was increased, the free –OH groups were occupied which increased the hydrophobicity of the nanocomposite scaffold. This not only decreased the amount of non-bounded water and % porosity but also caused a decrease in the pore size. Even though % porosity decreased, still the pore size of the nanocomposite scaffolds was in the range of 127–357 μm (Table 1), which was equal to/greater than the standard pore size of the ceramics (100–350 μm) required for better cell infiltration and cell adhesion.

3.5. Mechanical testing

Fig. 4 illustrates the stress–strain curves and young's modulus as a function of the GO. It is obvious from the figures that adding GO content increased the mechanical strength of the scaffolds. The Ultimate compression strength (UCS) increased from 3.90 Mpa for BgC-1.1 to 12.13 MPa for BgC-1.4, Young's modulus (Y) from 82.59 Mpa for BgC-1.1 to 394.87 MPa for BgC-1.4, and % strain from 9.23% for BgC-1.1 to 18.43 % for BgC-1.4 (Fig. 4A-B and Table 3). The composite scaffolds with 0.4 mg GO exhibited superior mechanical properties as compared to other scaffolds. The superior properties of the scaffold are attributed to the fact that GO has high surface energy and load-bearing properties which imparted better mechanical strength to the scaffolds. Hence, it is believed that the use of GO is suitable for applications in bone tissue engineering (Shin et al., 2016). UCS and % porosity are inverse to each other (Fig. 5C). Even though the % porosity and pore size decreased, still the pore size of the composite scaffolds is in the range as mentioned in the above sections. Mechanically stiff materials with roughness and appropriate porosity are adequate materials to facilitate bone repair by inducing cell responses like adhesion and proliferation.

3.6. Degradation

Fig. 5 shows the degradability of the nanocomposite scaffolds conducted in PBS under *in vitro* conditions (pH 7.4 and at 37 °C). *In vitro* degradation helps to understand the mechanism of scaffold degradation with time, which is very important for osteogenesis in bone tissue engineering. The composite scaffolds exhibited different degradation behavior with time (Fig. 5). Rapid and high degradation was observed for BgC-1.1, whereas slow and low degradation was observed for BgC-1.4. This trend of the degradation could be attributed to the glycosidic bonds dissociation of β-G, and BC (Kaur et al., 2018), and the weak interactions between the components of the nanocomposite scaffold in the case of BgC-1.1 and the strong interactions of the components of the BgC-1.4 (Berglund et al., 2019).

3.7. Swelling and water retention

Fig. 6 A shows the swelling ability of scaffolds determined in PBS solution and deionized water under *in-vitro* (pH 7.4 at 37 ℃) conditions. The swelling of the scaffolds is

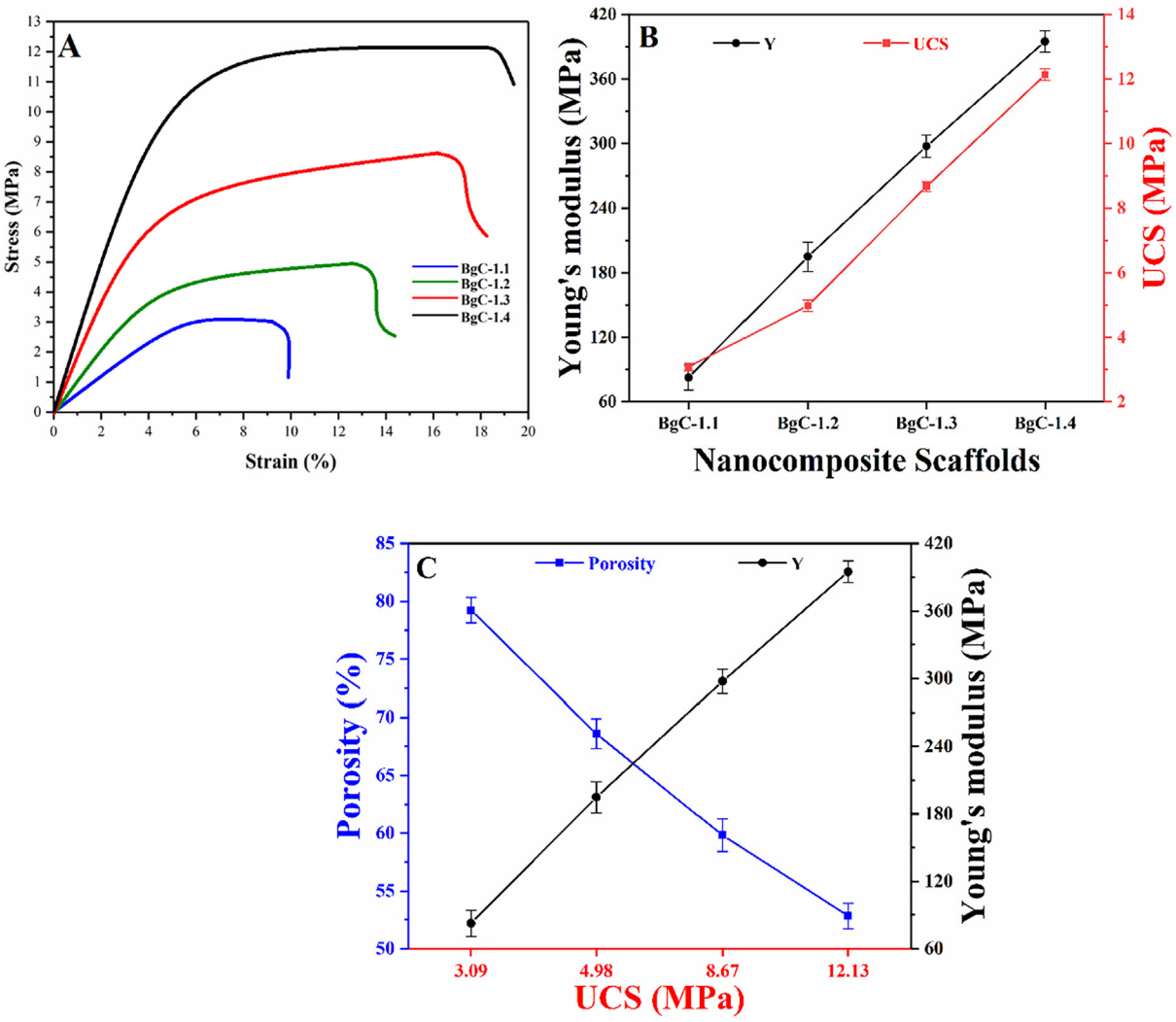

Fig. 4 Mechanical behavior of the composite scaffolds: (A) stress–strain curves, (B) young's modulus, and UCS, and (C) relationship of porosity with UCS and Young's modulus.

Table 3 Mechanical properties of the nanocomposite scaffold.

Sample	Young's modulus (MPa)	Ultimate compression strength (MPa)	Strain (%)	Crosslinking density (moL.m^{-3})
BgC-1.1	82.59 ± 1.5	3.90 ± 1.1	9.23 ± 1.5	0.011
BgC-1.2	194.85 ± 2.1	4.98 ± 1.3	12.76 ± 2.1	0.026
BgC-1.3	297.41 ± 2.2	8.67 ± 2.1	16.07 ± 1.1	0.040
BgC-1.4	394.87 ± 2.8	12.13 ± 2.4	18.43 ± 1.2	0.052

an important phenomenon in osteogenesis (due to the adhesion, propagation, and proliferation of *MC3T3-E1* cells) as swelling leads to the creation of pores and increases the porosity of the scaffolds that helps in cellular activity. Of the two media used, all the nanocomposite scaffold samples showed comparatively more swelling in an aqueous medium; though the composite scaffolds showed the same patterns in both media. The composite scaffold BgC-1.4 showed maximum swelling in both media. This increased swelling could be attributed partially to the electrostatic repulsion of the alcoholate and carboxylate groups of the polymeric matrix and GO, and partially to the slow and low degradation in both media (Namazi et al., 2019). The composite scaffold BgC-1.1 showed minimum swelling in both media. This behavior could be attributed to the presence of the lower carboxylate groups in the matrix (due to the low amount of the GO) and rapid and high degradation (due to weak interactions amongst components of the composite scaffold) in both media (Ghorpade., et al 2019). Fig. 6B shows the water retention ability of the composite scaffolds at different temperatures (35, 37, and 39 ℃). It is evident from the results that the composite scaffold BgC-1.4 retained more

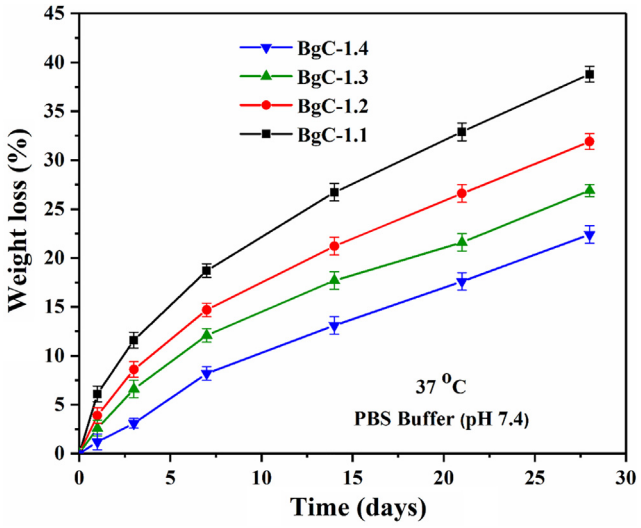

Fig. 5 Degradation of the nanocomposite scaffolds in PBS solution under *in vitro* (pH 7.4 and at 37 ℃).

water at all temperatures as compared to the other nanocomposite scaffolds. This is attributed to the formation of a less degradable composite network with an increased amount of GO, which did not allow water to flow out of the composite at all three temperatures (Depan et al., 2011; Stepien and Johnson, 2009; Qi, 2013). This behavior complements our argument stated above in favor of the better swelling of the BgC-1.4. The ability of a scaffold to regulate water retention capacity can be controlled by using various polymeric materials with specific water retention abilities. The lower retention of water by scaffolds results in dehydration and exudes accumulation in the wound. A polymer composite scaffold with sufficient water retention is, therefore, necessary to provide a moist environment to create the best bone regeneration microenvironment (Qi, 2013).

3.8. Antimicrobial activities

Antibacterial activities of scaffolds (BgC-1.1, BgC-1.2, BgC-1.3 & BgC-1.4) were analyzed against the severe infection-causing pathogens (*S. aureus,* E. coli, and *P. aeruginosa*) using disc diffusion method (Fig. 7). *S. aureus* is a pathogen that is known for causing osteomyelitis (infection in the bone), which can reach a bone by traveling through the blood stream or spreading from nearby tissue. This infection can also begin in the bone itself; if bone is exposed to this pathogen (Bereksi et al 2018; Pugazhendhi et al., 2018). The zones of inhibition against the pathogens for each scaffold extract were measured. It is evident from Fig. 7 that the zones of inhabitation increased as the amount of the GO was increased. The minimum zone of inhibition was observed for BgC-1.1 (~8 mm for *P. aeruginosa, ~7.5 mm for S. aureus,~ and 8.5 mm for* E. coli) scaffold and the maximum for BgC-1.4 (~17.7 mm for *P. aeruginosa, ~21.5 mm for S. aureus, and ~ 24. mm for* E. coli). The potential bonding of the lipophilic components (lipoproteins, liposaccharides, and phospholipids) of the pathogenic cell walls with nanocomposite scaffolds may be a combined effect of electrostatic and hydrophobic interactions. These interactions may vary with pathogens. For instance, scaffold BgC-1.1 zones of inhibition were ~ 8 mm for *P. aeruginosa,~7.5 mm for S. aureus,~ and 8.5 mm mm for* E. coli. Generally, the microorganisms adsorb and immobilized onto the surface of the hydrogels, and even the hydrogel may enter into the cells *via* the cytoplasmic membrane and binds to the ribosome of the pathogen to disrupt protein synthesis and hinder microbial activity (Doyle et al., 2019; Xie et al., 2020). Our discussion is also supported by increased WCA measurement.

3.9. In-vitro studies

3.9.1. SEM morphological analysis

The SEM morphologies of the MC3T3-E1 cells adhered to the nanocomposite scaffolds (BgC-1.1, BgC-1.2, BgC-1.3 & BgC-1.4) are shown in Fig. 8. To achieve successful clinical bone implant and mineralization, it is imperious to optimize cell

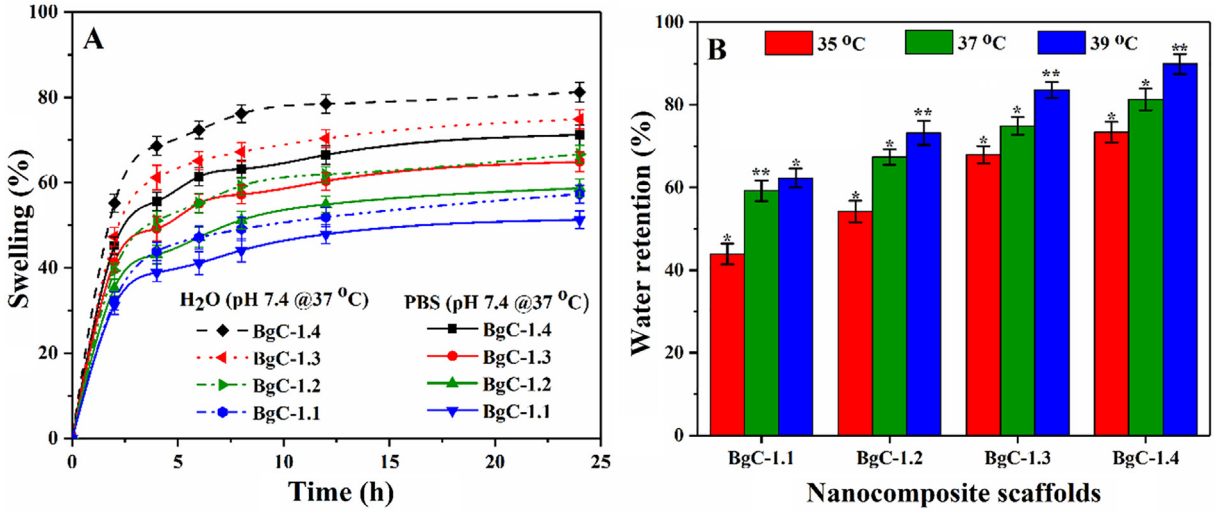

Fig. 6 Swelling kinetics of the nanocomposite scaffolds in aqueous and PBS media at 37 ℃ and (B) Water retention of the composite scaffolds at various temperatures (35, 37, 39 ℃). The pH of the media was 7.4.

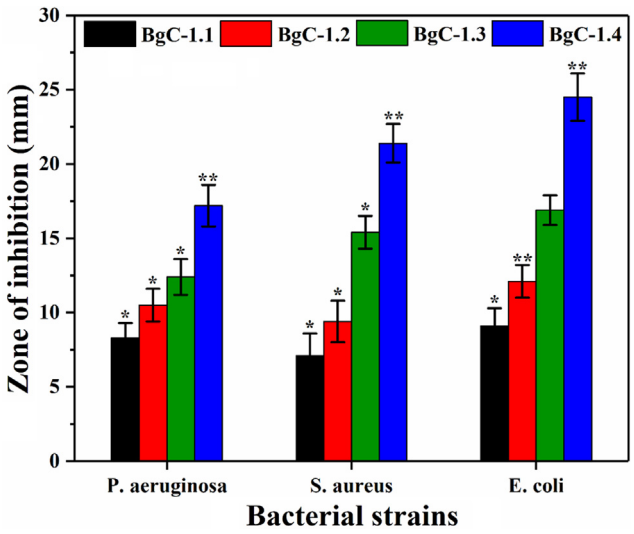

Fig. 7 Antibacterial activity (zones of inhibition) nanocomposite scaffolds against infection-causing pathogens.

adhesion, proliferation, and differentiation. The pre-osteoblast cell-cultured onto nanocomposite scaffolds for different time-periods (24, 48, 72 h) responded well by exhibiting good attachment and spreading all over the surface (Fig. 8). The adherence, proliferation, and propagation of the pre-osteoblast not only increased with time but also with the GO amount. This could be attributed to the fact that GO not only organized polymer chains but also form the irregular crumpled sheet into the polymer matrix. These crumpled sheets increased the roughness of the surface of the biocomposite. Rough surfaces give more sites for cell anchoring which also helps in the proliferation of cells (Tang et al., 2015). The other reason for the better adhesion of the cell to the composite is the superior mechanical properties with increased GO. Mechanically stiff materials are adequate to facilitate bone repair by inducing cells responses like adhesion and proliferation

3.9.2. Cell viability and optical density

Bone formation is a multi-steps process. Under *in-vitro* conditions stem cells undergo several morphologically different stages to become osteoblasts. The critical step in bone formation is proper cell adhesion to the matrix. Our scaffolds under

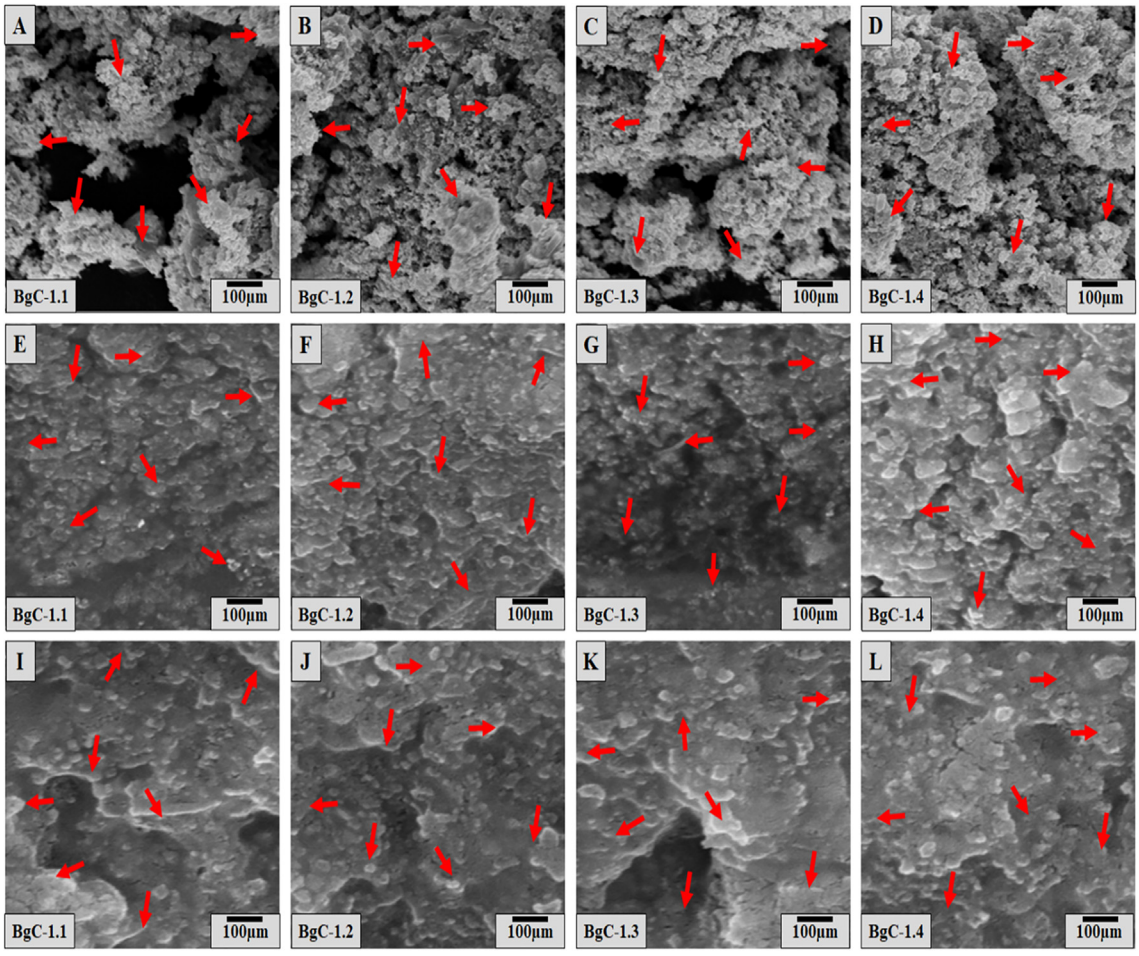

Fig. 8 SEM micrographs of the cell-cultured onto nanocomposite scaffolds. The micrographs were taken after 24 h (A, B, C, and D), 48 h (E, F, G, and H), and 72 h (I, J, K, and L). The red arrows indicate the pre-osteoblast cell adherence and proliferation of onto the composite scaffolds.

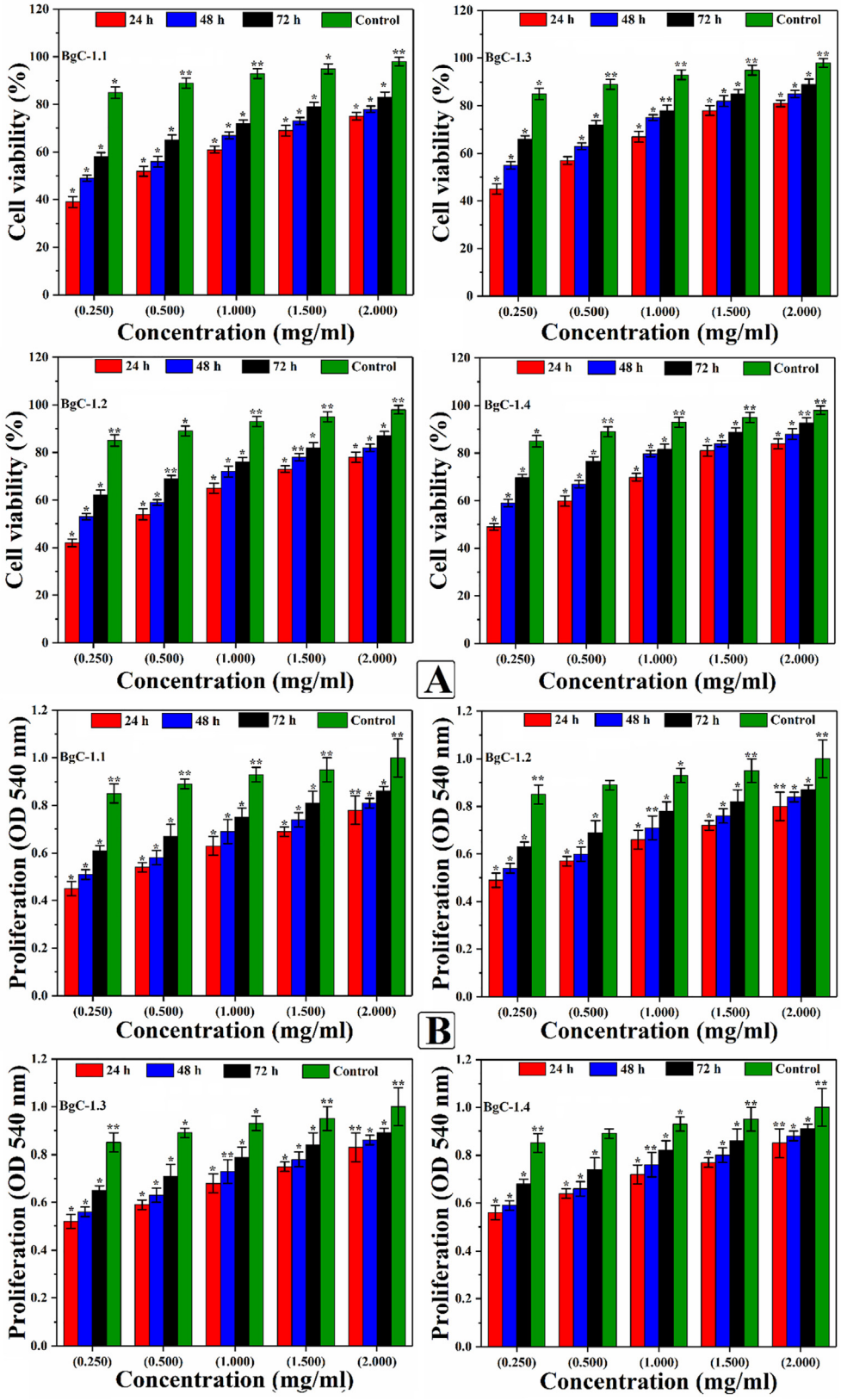

Fig. 9 Cell viability (A) and optical density of the proliferated cell (B) onto composite scaffolds: Gelatin-coating 0.1% was used as control. The percentage of cell viability in control was considered 100%. The mouse preosteoblast cells were seeded onto nanocomposite scaffolds using standard *in-vitro* conditions. The T-test significances value calculated for cell viability was $p < 0.001$ and optical density was $p < 0.05$.

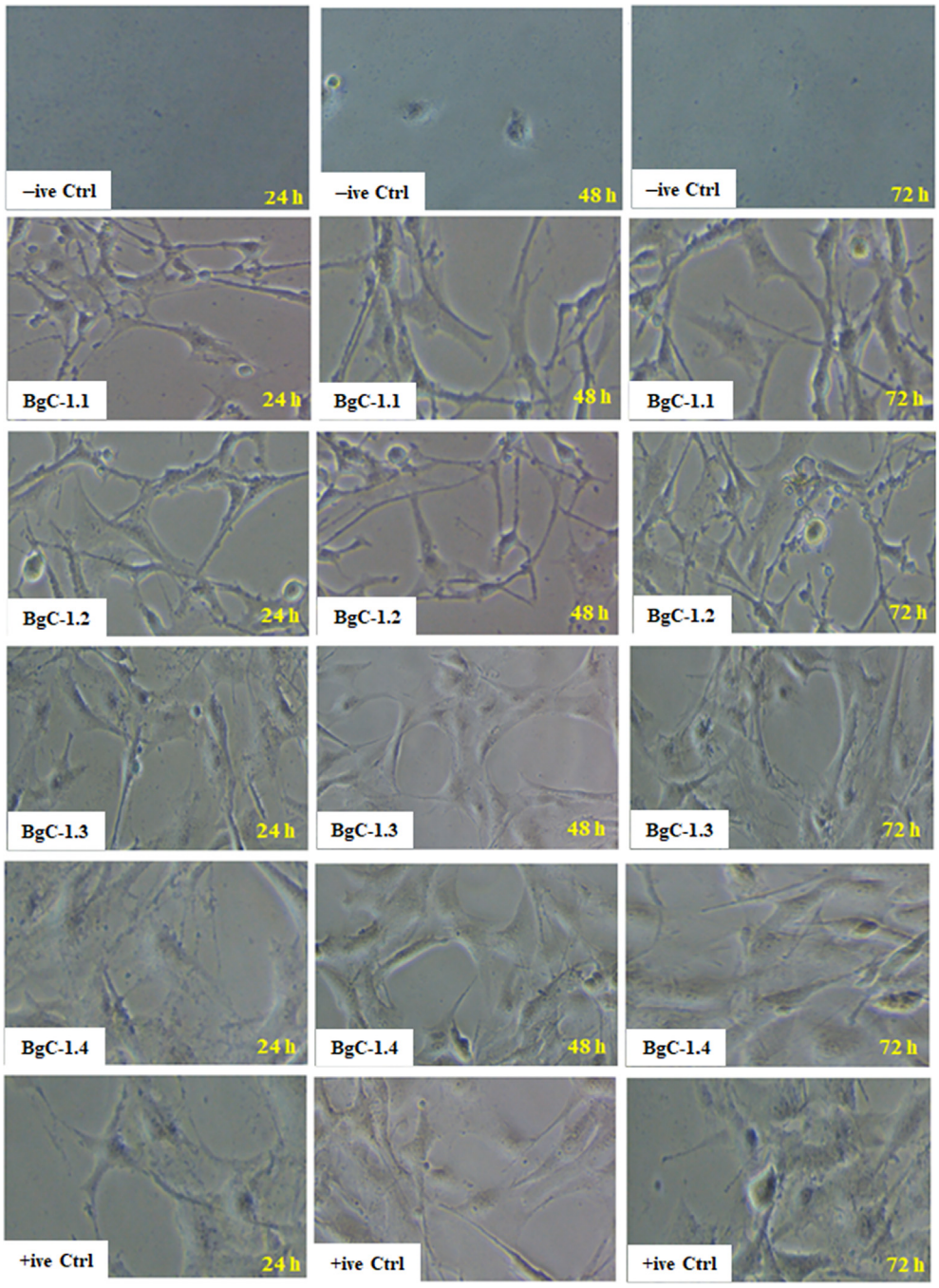

Fig. 10 Cell morphology of the MC3T3-E1 cell onto nanocomposited scaffolds, positive and negative controls at different time intervals (24, 48 & 72 h). Cells showed enhanced growth onto positive control after 72 h whereas no cell growth was observed onto negative control. Composite scaffolds BgC-1.4 and BgC-1.3 have shown similar cell behavior like a positive control.

study have shown potential for *MC3T3-E1* cells adhesion and proliferation. Comparing the results, we can see that almost all samples had good potential for cell adhesion and proliferation with very low cytotoxicity (Fig. 9A-B) (Khan et al., 2020a). These properties of our scaffolds are ideal for their potential use in bone formation under *in*-vitro conditions. The minor difference in the cell adhesion and proliferation between the samples may be attributed to the different physicochemical behavior of the scaffolds compared to positive control (0.1% gelatin)(Sigma Aldrich™). It is evident from Fig. 9A that BgC-1.4 has maximum cell viability, 93%, in comparison to positive control (gelatin) which has 100% cell viability. The order of the cell viability for the other samples was BgC-1.3 (79.8%) > BgC-1.2 (71.4%) > BgC-1.1 (68.9%). Similarly, the optical density of the proliferated cells was maximum for BgC-1.4 (Fig. 9B).

3.9.3. Cell morphology

Fig. 10 depicts the MC3T3-E1 cell morphologies cultured onto the nanocomposite scaffolds, positive (0.1% gelatin-coating) control, and negative (DMSO) control for 24 h, 48 h, 72 h. The attached cells showed ideal cell morphologies for the

MC3T3-E1 cells (cells were cylindrical) (Khan et al., 2020a,b,c). The cells adhered to the scaffolds BgC-1.1 and BgC-1.2 have shown relatively less retained thread like morphologies as compared to the positive control. No cells were observed onto negative control, as all cells died. It was also observed that increasing the amount of GO (BgC-1.3 and BgC-1.4), the cell morphology shifted towards regular cylindrical morphology from thin threads. The morphology of the cell was almost similar to the positive control. Thus, it is evident that increasing the amount of GO has a positive impact on cell adhesion, proliferation, and differentiation.

4. Conclusions

We have developed a nanocomposite scaffold for bone tissue engineering *via* free radical polymerization and freeze-drying technique using BC and β-G. n-HAp and GO were added as reinforcement materials. The structural changes, surface morphology, porosity, and mechanical properties were investigated through spectroscopic and analytical techniques like FT-IR, SEM, BET, and universal testing machine Instron. The scaffolds showed remarkable stability, aqueous degradation, spongy morphology, porosity, mechanical properties. Antibacterial activities were performed against gram-ve and gram + ve bacterial strains. The BgC-1.4 scaffold was found more antibacterial compared to BgC-1.3, BgC-1.2, and BgC-1.1. The cell culture and cytotoxicity were evaluated using the *MC3T3*-E1 cell line. More cell growth was observed onto BgC-1.4 due to its uniform interrelated pores distribution, surface roughness, better mechanical properties, considerable biochemical affinity towards cell adhesion, proliferation, and biocompatibility. These encouraging results support the applications of the scaffolds as an improved alternative for tissue engineering applications.

CRediT authorship contribution statement

Muhammad Umar Aslam Khan: Conceptualization, Data curation, Formal analysis, Investigation, Methodology, Software, Supervision, Validation, Visualization, Writing - original draft, Writing - review & editing. **Sajjad Haider:** Conceptualization, Data curation, Formal analysis, Funding acquisition, Investigation, Methodology, Project administration, Validation, Visualization, Writing - original draft, Writing - review & editing. **Adnan Haider:** Conceptualization, Data curation, Formal analysis, Investigation, Validation, Visualization, Methodology, Writing - review & editing. **Mohammed Rafiq Abdul Kadir:** Conceptualization, Resources. **Saiful Izwan Abd Razak:** Conceptualization, Funding acquisition, Project administration, Resources, Writing - original draft, Writing - review & editing. **Saqlain A Shah:** Methodology, Project administration, Resources, Supervision. **Aneela Javad:** Project administration, Software, Supervision, Validation. **Imran Shakir:** Writing - review & editing. **Ateyah A. Al-Zahrani:** Writing - review & editing.

Declaration of Competing Interest

The authors declare that they have no known competing financial interests or personal relationships that could have appeared to influence the work reported in this paper.

Acknowledgment

Authors from King Saud University would like to extend his sincere appreciation to the Deanship of Scientific Research (DSR) at King Saud University for its funding of this research through the Research Group no RG-1437-029

References

Askari, E., Cengiz, I., Alves, J., Henriques, B., Flores, P., Fredel, M., Mesquita-Guimarães, J., 2020. Micro-CT based finite element modelling and experimental characterization of the compressive mechanical properties of 3-D zirconia scaffolds for bone tissue engineering. J. Mech. Behav. Biomed. Mater. 102, 103516.

Aslam Khan, M.U., Mehboob, H., Abd Razak, S.I., Yahya, M.Y., Mohd Yusof, A.H., Ramlee, M.H., Amin, R., 2020. Development of Polymeric Nanocomposite (Xyloglucan-co-Methacrylic Acid/Hydroxyapatite/SiO2) Scaffold for Bone Tissue Engineering Applications—In-Vitro Antibacterial. Cytotoxicity and Cell Culture Evaluation. *Polymers* 12 (6), 1238.

Bauer, A., 1966. Kirby Bauer method antimicrobial susceptibility testing by a standardized single disk method. Am. J. Clin. Pathol. 45 (4), 493–496.

Bereksi, M.S., Hassaïne, H., Bekhechi, C., Abdelouahid, D.E., 2018. Evaluation of antibacterial activity of some medicinal plants extracts commonly used in Algerian traditional medicine against some pathogenic bacteria. Pharmacognosy Journal 10 (3).

Berglund, J., Azhar, S., Lawoko, M., Lindström, M., Vilaplana, F., Wohlert, J., Henriksson, G., 2019. The structure of galactoglucomannan impacts the degradation under alkaline conditions. Cellulose 26 (3), 2155–2175.

Caló, E., Khutoryanskiy, V.V., 2015. Biomedical applications of hydrogels: A review of patents and commercial products. Eur. Polym. J. 65, 252–267.

Chung, C., Kim, Y.-K., Shin, D., Ryoo, S.-R., Hong, B.H., Min, D.-H., 2013. Biomedical applications of graphene and graphene oxide. Acc. Chem. Res. 46 (10), 2211–2224.

Depan, D., Girase, B., Shah, J., Misra, R., 2011. Structure–process–property relationship of the polar graphene oxide-mediated cellular response and stimulated growth of osteoblasts on hybrid chitosan network structure nanocomposite scaffolds. Acta Biomater. 7 (9), 3432–3445.

Doyle, M.P., Diez-Gonzalez, F., Hill, C., 2019. Food microbiology: fundamentals and frontiers. John Wiley & Sons.

Fang, J., Li, P., Lu, X., Fang, L., Lü, X., Ren, F., 2019. A strong, tough, and osteoconductive hydroxyapatite mineralized polyacrylamide/dextran hydrogel for bone tissue regeneration. Acta Biomater. 88, 503–513.

Garg, K., Shanmugam, R., Ramamurthy, P.C., 2017. New covalent hybrids of graphene oxide with core modified and-expanded porphyrins: Synthesis, characterisation and their non linear optical properties. Carbon 122, 307–318.

General, S., & Welfare, C. S. (2013). Central statistics office.

Ghorpade, V.S., Dias, R.J., Mali, K.K., Mulla, S.I., 2019. Citric acid crosslinked carboxymethylcellulose-polyvinyl alcohol hydrogel films for extended release of water soluble basic drugs. J. Drug Delivery Sci. Technol. 52, 421–430.

Golafshan, N., Kharaziha, M., Fathi, M., Larson, B.L., Giatsidis, G., Masoumi, N., 2018. Anisotropic architecture and electrical stimulation enhance neuron cell behaviour on a tough graphene embedded PVA: alginate fibrous scaffold. RSC Adv. 8 (12), 6381–6389.

He, X., Liu, Y., Yuan, X., Lu, L., 2014. Enhanced healing of rat calvarial defects with MSCs loaded on BMP-2 releasing chitosan/alginate/hydroxyapatite scaffolds. PLoS ONE 9, (8) e104061.

Hu, C., Ashok, D., Nisbet, D.R., Gautam, V., 2019. Bioinspired surface modification of orthopedic implants for bone tissue engineering. Biomaterials 119366.

Huang, Y., Hao, M., Nian, X., Qiao, H., Zhang, X., Zhang, X., Zhang, H., 2016. Strontium and copper co-substituted hydroxyapatite-based coatings with improved antibacterial activity and cytocompatibility fabricated by electrodeposition. Ceram. Int. 42 (10), 11876–11888.

Kamal, H., Abd-Elrahim, F., Lotfy, S., 2014. Characterization and some properties of cellulose acetate-co-polyethylene oxide blends prepared by the use of gamma irradiation. J. Radiat. Res. Appl. Sci. 7 (2), 146–153.

Karahaliloglu, Z., Kilicay, E., Denkbas, E.B., 2017. Antibacterial chitosan/silk sericin 3D porous scaffolds as a wound dressing material. Artif. Cells Nanomed. Biotechnol. 45 (6), 1172–1185.

Kaur, M., Kaur, M., Sharma, V.K., 2018. Nitrogen-doped graphene and graphene quantum dots: A review onsynthesis and applications in energy, sensors and environment. Adv. Colloid Interface Sci. 259, 44–64.

Khan, M.U.A., Al-Thebaiti, M.A., Hashmi, M.U., Aftab, S., Abd Razak, S.I., Abu Hassan, S., Amin, R., 2020a. Synthesis of Silver-Coated Bioactive Nanocomposite Scaffolds Based on Grafted Beta-Glucan/Hydroxyapatite via Freeze-Drying Method: Anti-Microbial and Biocompatibility Evaluation for Bone Tissue Engineering. Materials 13 (4), 971.

Khan, M.U.A., Haider, S., Shah, S.A., Abd Razak, S.I., Hassan, S.A., Kadir, M.R.A., Haider, A., 2020b. Arabinoxylan-co-AA/HAp/TiO2 nanocomposite scaffold a potential material for bone tissue engineering: An in vitro study. Int. J. Biol. Macromol. 151, 584–594.

Khan, M.U.A., Raza, M.A., Mehboob, H., Kadir, M.R.A., Abd Razak, S.I., Shah, S.A., Amin, R., 2020c. Development and in vitro evaluation of κ-carrageenan based polymeric hybrid nanocomposite scaffolds for bone tissue engineering. RSC Adv. 10 (66), 40529–40542.

Khan, M. U. A., Raza, M. A., Razak, S. I. A., Abdul Kadir, M. R., Haider, A., Shah, S. A., . . . Aftab, S., Novel Functional Antimicrobial and Biocompatible Arabinoxylan/Guargum Hydrogel for Skin Wound Dressing Applications. Journal of Tissue Engineering and Regenerative Medicine.

Liu, R., Liang, S., Tang, X.-Z., Yan, D., Li, X., Yu, Z.-Z., 2012. Tough and highly stretchable graphene oxide/polyacrylamide nanocomposite hydrogels. J. Mater. Chem. 22 (28), 14160–14167.

Long, N.T., Anh, N.T.N., Giang, B.L., Son, H.N., Luan, L.Q., 2019. Radiation Degradation of β-Glucan with a Potential for Reduction of Lipids and Glucose in the Blood of Mice. Polymers 11 (6), 955.

Maheshwari, S.U., Samuel, V.K., Nagiah, N., 2014. Fabrication and evaluation of (PVA/HAp/PCL) bilayer composites as potential scaffolds for bone tissue regeneration application. Ceram. Int. 40 (6), 8469–8477.

Masters, E.A., Trombetta, R.P., de Mesy Bentley, K.L., Boyce, B.F., Gill, A.L., Gill, S.R., Ito, H., 2019. Evolving concepts in bone infection: redefining "biofilm", "acute vs. chronic osteomyelitis", "the immune proteome" and "local antibiotic therapy". Bone Res. 7 (1), 1–18.

Modrogan, C., Pandele, A.M., Bobirică, C., Dobrotă, D., Dăncilă, A. M., Gârleanu, G., Orbeci, C., 2020. Synthesis, Characterization and Sorption Capacity Examination for a Novel Hydrogel Composite Based on Gellan Gum and Graphene Oxide (GG/GO). Polymers 12 (5), 1182.

Muruganandi, G., Saravanan, M., Vinitha, G., Raj, M.J., Girisun, T.S., 2018. Barium borate nanorod decorated reduced graphene oxide for optical power limiting applications. Opt. Mater. 75, 612–618.

Namazi, H., Hasani, M., Yadollahi, M., 2019. Antibacterial oxidized starch/ZnO nanocomposite hydrogel: synthesis and evaluation of its swelling behaviours in various pHs and salt solutions. Int. J. Biol. Macromol. 126, 578–584.

Pugazhendhi, A., Prabakar, D., Jacob, J.M., Karuppusamy, I., Saratale, R.G., 2018. Synthesis and characterization of silver nanoparticles using Gelidium amansii and its antimicrobial property against various pathogenic bacteria. Microb. Pathog. 114, 41–45.

Qi, Z., 2013. Water retention and drainage on air side of heat exchangers—A review. Renew. Sustain. Energy Rev. 28, 1–10.

Repetto, G., Del Peso, A., Zurita, J.L., 2008. Neutral red uptake assay for the estimation of cell viability/cytotoxicity. Nat. Protoc. 3 (7), 1125.

Riahi, N., Liberelle, B., Henry, O., De Crescenzo, G., 2017. Impact of RGD amount in dextran-based hydrogels for cell delivery. Carbohydr. Polym. 161, 219–227.

Sancilio, S., Gallorini, M., Di Nisio, C., Marsich, E., Di Pietro, R., Schweikl, H., & Cataldi, A. (2018). Alginate/hydroxyapatite-based nanocomposite scaffolds for bone tissue engineering improve dental pulp biomineralization and differentiation. Stem Cells International, 2018.

Saravanan, S., Chawla, A., Vairamani, M., Sastry, T., Subramanian, K., Selvamurugan, N., 2017. Scaffolds containing chitosan, gelatin and graphene oxide for bone tissue regeneration in vitro and in vivo. Int. J. Biol. Macromol. 104, 1975–1985.

Shah, S.A., Khan, M.A., Arshad, M., Awan, S., Hashmi, M., Ahmad, N., 2016. Doxorubicin-loaded photosensitive magnetic liposomes for multi-modal cancer therapy. Colloids Surf., B 148, 157–164.

Shin, S.R., Zihlmann, C., Akbari, M., Assawes, P., Cheung, L., Zhang, K., Wan, K.t., 2016. Reduced graphene oxide-gelMA hybrid hydrogels as scaffolds for cardiac tissue engineering. Small 12 (27), 3677–3689.

Skrabl-Baumgartner, A., Singer, P., Greimel, T., Gorkiewicz, G., Hermann, J., 2019. Chronic non-bacterial osteomyelitis: a comparative study between children and adults. Pediatric Rheumatology 17 (1), 49.

Soundarya, S.P., Menon, A.H., Chandran, S.V., Selvamurugan, N., 2018. Bone tissue engineering: Scaffold preparation using chitosan and other biomaterials with different design and fabrication techniques. Int. J. Biol. Macromol. 119, 1228–1239.

Srivastava, A., Kumar, R., 2013. Synthesis and characterization of acrylic acid-g-(-carrageenan) copolymer and study of its application. International Journal of Carbohydrate Chemistry.

Stepien, P., Johnson, G.N., 2009. Contrasting responses of photosynthesis to salt stress in the glycophyte Arabidopsis and the halophyte Thellungiella: role of the plastid terminal oxidase as an alternative electron sink. Plant Physiol. 149 (2), 1154–1165.

Tang, Y., Hu, H., Zhang, M.G., Song, J., Nie, L., Wang, S., Chen, X., 2015. An aptamer-targeting photoresponsive drug delivery system using "off–on" graphene oxide wrapped mesoporous silica nanoparticles. Nanoscale 7 (14), 6304–6310.

Thévenin-Lemoine, C., Vial, J., Labbé, J.-L., Lepage, B., Ilharreborde, B., Accadbled, F., 2016. MRI of acute osteomyelitis in long bones of children: pathophysiology study. Orthopaedics & Traumatology: Surgery & Research 102 (7), 831–837.

Todica, M., Stefan, T., Simon, S., Balasz, I., Daraban, L., 2014. UV-vis and XRD investigation of graphite-doped poly (acrylic) acid membranes. Turkish Journal of Physics 38 (2), 261–267.

Torgbo, S., Sukyai, P., 2018. Bacterial cellulose-based scaffold materials for bone tissue engineering. Appl. Mater. Today 11, 34–49.

Ullah, H., Santos, H.A., Khan, T., 2016. Applications of bacterial cellulose in food, cosmetics and drug delivery. Cellulose 23 (4), 2291–2314.

Unnithan, A.R., Sasikala, A.R.K., Park, C.H., Kim, C.S., 2017. A unique scaffold for bone tissue engineering: An osteogenic combination of graphene oxide–hyaluronic acid–chitosan with simvastatin. J. Ind. Eng. Chem. 46, 182–191.

Wiggli, B.J., Frei, R., Laffer, R., Tschudin Sutter, S., Widmer, A.F.-X., 2017. Survival from methicillin-sensitive Staphylococcus aureus bloodstream infections over 20 years: a cohort of 1328 patients. Swiss Medical Weekly 147 (3940).

Wood, P.J., Weisz, J., Fedec, P., Burrows, V.D., 1989. Large-scale preparation and properties of oat fractions enriched in (1–3)(1–4)-β-D-glucan. Cereal Chemistry 66 (2), 97–103.

Wright, M.E., Wong, A.T., Levitt, D., Parrag, I.C., Yang, M., Santerre, J.P., 2018. Influence of ciprofloxacin-based additives on the hydrolysis of nanofiber polyurethane membranes. J. Biomed. Mater. Res. Part A 106 (5), 1211–1222.

Xie, Y.-Y., Hu, X.-H., Zhang, Y.-W., Wahid, F., Chu, L.-Q., Jia, S.-R., Zhong, C., 2020. Development and antibacterial activities of bacterial cellulose/graphene oxide-CuO nanocomposite films. Carbohydr. Polym. 229, 115456.

Yamanaka, S., Watanabe, K., Kitamura, N., Iguchi, M., Mitsuhashi, S., Nishi, Y., Uryu, M., 1989. The structure and mechanical properties of sheets prepared from bacterial cellulose. J. Mater. Sci. 24 (9), 3141–3145.

Yuan, Y., Zhang, G., Li, Y., Zhang, G., Zhang, F., Fan, X., 2013. Poly (amidoamine) modified graphene oxide as an efficient adsorbent for heavy metal ions. Polym. Chem. 4 (6), 2164–2167.